

ITEP conception of a heavy ion fusion facility

Mikhail M. Basko, Mikhail D. Churazov, Dimitri G. Koshkarev

Institute for Theoretical and Experimental Physics, B. Cheremushkinskaya 25, 117259 Moscow, Russia

Abstract

A conceptual scheme is presented which combines self-consistently a hohlraum target design at the input energy $E_{dr} = 10$ MJ with a scheme for a charge-symmetric heavy ion driver capable of producing the pulse power profile and the focal spot size required for target ignition and high energy gain. The physical issues underlying the key aspects of the target performance are put together into a coherent theoretical scheme which allows the target parameters to be rescaled to other values of E_{dr} . Special attention is paid to the method of pulse shaping in the final stages of beam compression by taking advantage of four different platinum isotopes employed in the driver scheme. It is found that a heavy ion fusion facility designed along the same lines for a considerably lower input energy $E_{dr} \approx 2$ MJ would require a power pulse of 2.5–3 ns, which appears to be prohibitively short for present accelerator technology.

1. Introduction

A steady progress in experimenting with laser-driven hohlraum implosions at the Livermore Nova facility has led the US inertial confinement fusion (ICF) programme to focus on achieving thermonuclear ignition with 1–2 MJ of laser energy within the next decade [1,2]. Naturally, a question arises what the accelerator parameters and the target design should be that would lead to ignition at a minimum energy scale in heavy ion inertial fusion (HIF) approach. Unfortunately, no implosion experiments driven either directly or indirectly by beams of heavy ions have been conducted so far. Hence, a consistent conceptual project should rely on earlier experience in designing and building ion accelerators and on the hohlraum implosion database accumulated within the laser ICF programme. Previous HIF system

studies [3,4] employed direct drive target schemes, but did not address adequately the issues of symmetry and stability of the fuel implosion. Although it would possibly be premature to rule direct drive out entirely, a general consensus today is that the most practical way to ignition in HIF lies with the indirect drive approach. The indirect drive has such important advantages as an easier irradiation geometry and a possibility to benefit from the experimental results on laser-driven hohlraum implosions [5].

Here we present a conceptual scheme of a driver–target system for an HIF facility, which we believe to be both realistic and self-consistent in at least its principal aspects, and which reflects the present status of heavy ion fusion research at the Institute for Theoretical and Experimental Physics in Moscow. In section 2 the basic assump-

tions and relationships are formulated which enable us to evaluate the parameters of an indirect drive hohlraum target designed for a given value of the input energy E_{dr} . The overall target performance is simulated within the framework of a one-dimensional (1D) three-temperature hydrodynamics model. Section 3 describes the principal scheme of the accelerator–storage complex, based on the method of charge compensation in the final beam transport line [6], which is capable of producing the power pulse and the focal spot size required for ignition and high energy gain at $E_{dr} = 10$ MJ. We find that an HIF facility designed along the same lines for a considerably lower input energy $E_{dr} \approx 2$ MJ would require a prohibitively short main pulse duration, i.e. $t_{mp} \approx 2.5$ ns.

2. Target design

In this section we describe the principle of an indirect drive hohlraum-type target designed for the input energy $E_{dr} = 10$ MJ. However, all the calculations can be readily repeated for other values of E_{dr} as well. The key aspects of the target performance are analysed separately, with no integrated two-dimensional (2D) (or three-dimensional (3D)) simulations of its overall performance carried out so far.

2.1. Symmetrization in the hohlraum

The principal task of the hohlraum design is to ensure adequate symmetry of irradiation of the central fusion capsule by thermal X-rays. Here we argue that such symmetry can most readily be obtained in hohlraums with case-to-capsule surface area ratios $S_{case}/S_{caps} \approx 25$ –30.

Consider a cylindrical hohlraum of radius R_{case} with a spherical fusion capsule of radius R_{caps} in its centre (Fig. 1). Suppose that the capsule surface is irradiated with thermal X-rays emitted by two bright circular bands on the inner wall of the hohlraum, each band of width h_c and symmetric with respect to its counterpart across the equatorial plane. The rest of the casing wall surface is assumed to be black. Clearly, the non-uniformity

of the incident X-ray flux over the capsule surface contains only even Legendre modes. The elevation z_c of the bright ring above the equatorial plane can always be chosen such as to eliminate the $l=2$ mode. Depending on the value of h_c/R_{case} , this occurs at a value of the illumination angle $\alpha_c \equiv \arctan [(z_c + \frac{1}{2}h_c)/R_{case}]$ close to 33° – 36° . Also, the second free parameter of the hohlraum geometry, the case-to-capsule radius ratio R_{case}/R_{caps} , can always be adjusted such as to eliminate the next $l=4$ mode. Fig. 2 shows how the $l=2$ and $l=4$ modes vanish simultaneously at $R_{case}/R_{caps} = 4.55$ for $h_c = 0$ and at $R_{case}/R_{caps} = 4.36$ for $h_c/R_{case} = 0.7$. If we assume that a cylindrical hohlraum has a minimum length $L_{case} = 2(z_c + h_c)$ which still accommodates the shining bands of width h_c , we find that the case-to-capsule area ratio S_{case}/S_{caps} varies between 23.4 and 29.7 as the value of h_c changes from 0 to $0.7R_{case}$. The amplitude of the first non-vanishing mode $l=6$ is less than about 1.5% (whenever $h_c \geq 0.3R_{case}$). If we solve the same problem for a spherical hohlraum, we find that the $l=4$ mode vanishes at

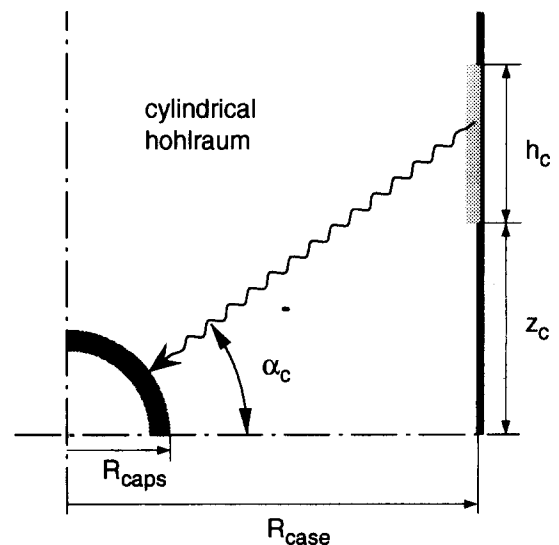


Fig. 1. Schematic view of a cylindrical hohlraum of radius R_{case} with a spherical fusion capsule of radius R_{caps} in its centre. The uniformity of capsule irradiation is evaluated for $t=0$, by assuming that thermal X-rays are emitted by two uniformly heated circular bands of height h_c along the hohlraum wall, placed symmetrically with respect to the equatorial plane.

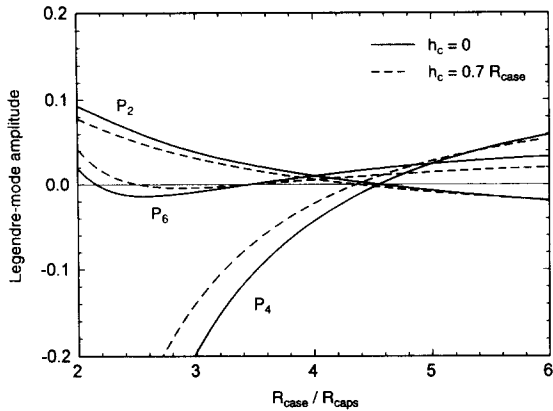


Fig. 2. Amplitudes of the first three even Legendre modes in the brightness distribution over the capsule surface vs. the ratio $R_{\text{case}}/R_{\text{caps}}$ between the casing and the capsule radii for the irradiation scheme shown in Fig. 1. Two extreme cases of infinitely narrow ($h_c = 0$, —) and relatively broad ($h_c = 0.7R_{\text{case}}$, ---) bright bands are presented. In each of these cases, the illumination angle $\alpha_c = \arctan[(z_c + \frac{1}{2}h_c)/R_{\text{case}}]$ was kept fixed at a value that ensured simultaneous vanishing of the $l = 2$ and $l = 4$ modes ($\alpha_c = 32^\circ 51'$ for $h_c = 0$, and $\alpha_c = 35^\circ 30'$ for $h_c = 0.7R_{\text{case}}$).

$R_{\text{case}}/R_{\text{caps}} = 4.96$ independently of the value of h_c , i.e. at $S_{\text{case}}/S_{\text{caps}} = 25$. A remarkable fact is that the optimal value of $R_{\text{case}}/R_{\text{caps}}$ defined in this way is rather insensitive to the brightness distribution over the shining bands on the hohlraum wall.

The above results correspond to a “snapshot” picture at time $t = 0$ of a sudden turn-on of the X-ray source. As time goes on, two main effects take place. First of all, the remainder of the casing wall heats up and the $l = 6$ and all higher modes decay in time by a substantial factor (more detailed results on this will be presented elsewhere); as a consequence, these modes can be ignored altogether. Secondly, the casing wall and the capsule ablator undergo hydrodynamic expansion, so that their “optical” boundaries change position and become smeared. As a result, the hohlraum geometry changes in time, and the amplitudes of the $l = 2$ and $l = 4$ modes deviate from zero. A proper simulation of this effect requires at least a 2D hydrodynamics code with full account of the spectral radiative transfer because the approximation of sharp re-emitting surfaces becomes inadequate. Nevertheless, we believe that the results presented in Fig. 2 provide good evidence that the

$l = 2$ and 4 modes of the time-integrated asymmetries in the DT fuel implosion can be simultaneously put to zero in a cylindrical hohlraum with the initial proportion $R_{\text{case}}/R_{\text{caps}} \approx 4$. Accordingly, when modelling a 3D hohlraum target with an “energetically equivalent” 1D configuration, we assume a fixed value of the initial case-to-capsule area ratio $S_{\text{case}}/S_{\text{caps}} = 25$, which approximates a cylindrical hohlraum of length $L_{\text{case}} \approx 2(z_c + h_c)$ with $h_c \approx 0.3R_{\text{case}}$.

2.2. Converter material

The energy of irradiating ion beams is converted into thermal X-rays in the X-ray converters placed inside the hohlraum. The main energy losses are associated with the thermal energy of the converter material and the heating wave which propagates into the hohlraum wall. The kinetic energy of an expanding converter can usually be made small by restraining its sideward expansion and by adopting large enough initial dimensions.

Thus, the relevant physical quantities which determine the optimal choice of the converter material are its specific heat, stopping power for the beam ions, and opacity. Assuming that the converter consists of some base low Z element doped with a small amount of high Z material, we can vary its opacity independently of the specific heat and stopping power. As it turns out, in this way we can keep the optical thickness of the converter near its optimum value for different base elements. Suppose for simplicity that the dimensions and the geometry of the converter are fixed, and we have adopted a certain tolerance level for the energy that is to be spent to heat up the converter to its working temperature T_{con} . This means that the inertial energy per unit volume of the converter given by

$$\rho \epsilon_{\text{con}} = n Z T_{\text{con}} \left[\frac{3}{2} (1 + Z^{-1}) + \frac{E_{\text{iz}}}{Z T_{\text{con}}} \right] \quad (1)$$

is fixed. Here Z and n are respectively the atomic number and the number density of the base converter element and E_{iz} is its total ionization energy per atom (a posteriori, one readily verifies that the base converter material is practically fully ionized under the conditions of interest). Clearly, the best

Table 1
Values of $f(Z, T_{\text{con}})$ for different Z and two values of T_{con}

Z	1	2	3	4	5	6
$f(Z, T_{\text{con}})$						
$T_{\text{con}} = 200$ eV	3.068	2.447	2.339	2.373	2.471	2.608
$T_{\text{con}} = 300$ eV	3.045	2.579	2.226	2.208	2.247	2.322

choice for Z will be the one which yields the highest value of the stopping power for the beam ions, i.e.

$$-\frac{dE_b}{dx} = \frac{4\pi Z_{\text{eff}}^2}{m_e v_b^2} nZ \ln \frac{2m_e v_b^2}{h\omega_p} \propto \frac{\ln[C_1(T_{\text{con}}f)^{1/2}]}{T_{\text{con}}f} \quad (2)$$

at a given value of $\rho\epsilon_{\text{con}} = nZT_{\text{con}}f$; here v_b is the velocity of beam ions, Z_{eff} is their effective charge (whose dependence on Z and T_{con} can, to a first approximation, be ignored), $\omega_p = (4\pi e^2 nZ/m_e)^{1/2}$ is the plasma frequency of the converter, and C_1 is a constant (with respect to Z and T_{con} variations) not significant for the present argument. It is a simple exercise to show that, with respect to variations in Z , the maximum of $|dE_b/dx|$ coincides with the minimum of the function

$$f(Z, T_{\text{con}}) = \frac{3}{2}(1 + Z^{-1}) + \frac{E_{iz}}{ZT_{\text{con}}} \quad (3)$$

provided that the Coulomb logarithm $\ln(2m_e v_b^2/h\omega_p) > \frac{1}{2}$.

From Table 1 we see that the function $f(Z, T_{\text{con}})$ has a minimum at $Z = 3$ for $T_{\text{con}} = 200$ eV, and at $Z = 4$ for $T_{\text{con}} = 300$ eV. Accordingly, we choose beryllium as the base element for the converter material. Earlier, beryllium converters for heavy ion targets have been studied by Ho et al. [7]. Note that, although we used the quantum Larkin [8] formula in Eq. (2) to evaluate the stopping power of plasma electrons, the final result can be rederived in the case of classical Coulomb scattering as well.

2.3. Converter mass and the beam-to-capsule energy coupling

The fraction δ_{con} of the driver energy that is afforded to heat up the converter material is essentially a free parameter (within certain limits)

of the hohlraum target design. Given the driver energy E_{dr} , this parameter determines the total converter mass and can be chosen more or less arbitrarily. The larger the converter mass, the less efficient is the target; the smaller the converter mass, the more stringent become constraints on the final focus of the ion beams. As a reasonable compromise, we adopt the value

$$\delta_{\text{con}} = \frac{E_{\text{con}}}{E_{\text{dr}}} = 0.2$$

Then, the total converter mass M_{con} can be evaluated by invoking the specific heat of the fully ionized beryllium:

$$\begin{aligned} E_{\text{con}} &= M_{\text{con}} \epsilon_{\text{Be}}(T_{\text{con}}) \\ &= M_{\text{con}} [0.08(T_{\text{con}} + 53.2 \text{ eV}) \text{ MJ g}^{-1}] \quad (4) \end{aligned}$$

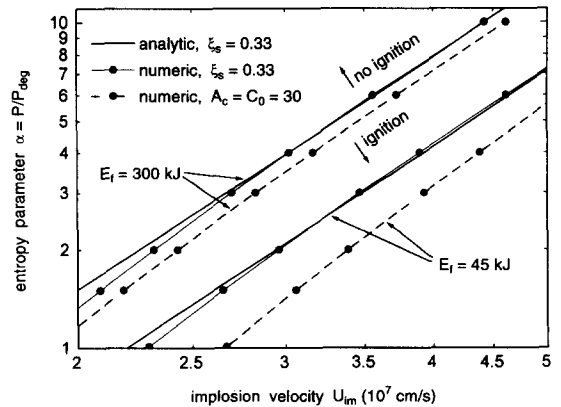


Fig. 3. Ignition boundaries in the (U_{im}, α) parametric plane for two values of the energy E_f invested into the fuel: —, the limiting scaling law (15); -●- 1D 2-T simulations starting from the optimal assembled fuel states; -●- 1D 3-T simulations carried out under the additional constraints of fixed values of the inflight aspect ratio (IFAR) $A_f = 30$ and the radial convergence ratio $C_0 = 30$.

For $E_{dr} = 10$ MJ and $T_{con} = 300$ eV we obtain $M_{con} = 70$ mg.

Once the converter mass and material as well as the hohlraum proportions are fixed, we can calculate the energy coupling efficiency η_{caps} between the ion beams and the fusion capsule by using the 1D code. This important parameter can be expressed as

$$\eta_{caps} = (1 - \delta_{con}) \frac{S_{caps} \int F_{caps} dt}{S_{caps} \int F_{caps} dt + S_{case} \int F_{case} dt} = \frac{(1 - \delta_{con}) f_{ac}}{f_{ac} + S_{case}/S_{caps}} \quad (5)$$

where

$$f_{ac} = \int F_{caps} dt / \int F_{case} dt \quad (6)$$

is the ratio between the time-integrated net absorbed X-ray fluxes per unit area of the capsule and casing surfaces (the hohlraum is assumed to have no holes, so that all the X-ray energy emitted by the converters is absorbed by the capsule and the casing walls). The flux ratio f_{ac} depends on the X-ray temperature history and materials chosen for the casing wall and the capsule ablator. 1D simulations performed for the gold casing and beryllium ablator, configured as shown below in Fig. 5, yielded $f_{ac} = 8.5$ for a 10 MJ, 1000 TW pulse, which heats the hohlraum cavity to $T_x = 210$ eV. Hence, in a hohlraum target with $S_{case}/S_{caps} \approx 25$ driven by a 10 MJ ion pulse we can count on an energy coupling efficiency $\eta_{caps} \approx 20\%$.

It should be noted here that this estimate of η_{caps} does not allow for the beam energy losses in the converter lids: thin (some 15 μm for 10 GeV ^{209}Bi ions) layers of gold covering the converters from outside along the beam path. Separate 1D runs carried out to explore this effect have shown that, in the optimum case, these additional losses consume some 15% of the total beam energy E_{dr} .

2.4. Gain model and target dimensions

Given the driver energy E_{dr} and having evaluated the beam-to-capsule transfer efficiency η_{caps} ,

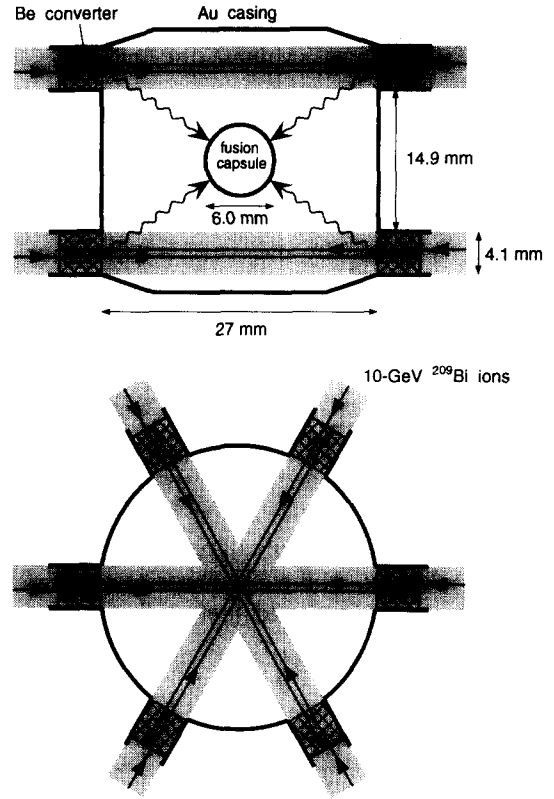


Fig. 4. Cut-away front and top views of a three-dimensional hohlraum target with 12 converter pockets and no radiation shields. Each of the 12 ion beams passes through the hohlraum and leaves its energy in two converter pockets on opposite sides of the hohlraum wall. The target dimensions correspond to the input energy $E_{dr} = 10$ MJ.

we find the energy $E_{caps} = \eta_{caps} E_{dr}$ which enters the central fusion capsule. In this subsection we present the guidelines along which one can, for a given value of E_{caps} , design a fusion capsule that would perform close to the optimum.

First of all, we assume that the hydrodynamic efficiency of ablation by thermal X-rays is close to its optimal value $\eta_h \approx 18\%$ [9]. This value agrees well with the results of 1D simulations discussed below. Assuming that the capsule ablator is almost fully evaporated by the end of implosion, we calculate the energy

$$E_f = \eta_h E_{caps} = \eta_h \eta_{caps} E_{dr} \quad (7)$$

that is transferred to the fuel. Given this energy,

we can use a simplified gain model based on the analysis of assembled fuel states in the desired mode of ignition to evaluate the fuel mass and other capsule parameters.

Here we employ the gain model described in Ref. [10], which is based on the hydrodynamically consistent self-similar pressure and density profiles near the time of ignition. We assume that the DT fuel is ignited by means of a thermonuclear spark in its centre at the time of maximum compression. Then, the fuel state at ignition can be fully specified by the values of the following five parameters: T_s (keV), spark temperature; H_s (g cm⁻²), spark $\langle or \rangle$; U_{im} (10⁷ cm s⁻¹), implosion velocity; $\xi_s = R_s/R_f$, fractional spark radius; $\alpha = P/P_{deg}$, entropy parameter of the cold fuel defined as the ratio between the actual DT pressure and the Fermi pressure of fully degenerate electrons at the same density. The parameter α is assumed to be constant over the cold fuel shell. In terms of these parameters, the energy invested into the fuel can be expressed as [10]

$$E_f \text{ (MJ)} = 0.813 \frac{\alpha^3 (H_s T_s)^3}{U_{im}^{10}} A_E \quad (8)$$

where

$$A_E = \frac{[1 - (2\Omega)^{-1} \xi_s^2]^3 (\phi_E)^5 \left(\phi_E + \frac{128}{75} \frac{\xi_s^5}{\Omega - \frac{1}{2} \xi_s^2} \right)}{\xi_s^3 (1 - \xi_s^2)^5 (\phi_M)^5} \quad (9)$$

is a function of ξ_s and of the dimensionless constant $\Omega \geq 1$ which characterizes the density jump between the spark and the main fuel. Eq. (9) originates from integration over the analytical density profile of the self-similar solution. A graphical representation of the function $A_E(\Omega, \xi_s)$ is given elsewhere in this volume [11]. When expressed in terms of the basic model parameters, the value of Ω is given by

$$\Omega = 2.9 \frac{T_s \phi_E}{U_{im}^2 \phi_M} \quad (10)$$

where

$$\phi_M = \frac{\pi/2 - \arcsin \xi_s}{(1 - \xi_s^2)^{5/2}} + \frac{\xi_s}{3} \frac{8\xi_s^4 - 14\xi_s^2 + 3}{(1 - \xi_s^2)^2} \quad (11)$$

$$\phi_E = \frac{\pi/2 - \arcsin \xi_s}{(1 - \xi_s^2)^{5/2}} + \frac{\xi_s}{3} \frac{16\xi_s^6 - 24\xi_s^4 + 2\xi_s^2 + 3}{(1 - \xi_s^2)^2} \quad (12)$$

are slowly varying monotonic functions of ξ_s only. To the accuracy that the fuel mass fraction in the spark can be neglected, the total fuel mass

$$M_f = 2E_f/U_{im}^2. \quad (13)$$

In fact, this relationship serves as a definition of U_{im} .

The function $A_E(\xi_s, \Omega)$ is very insensitive to the values of Ω for $\Omega \approx 1-3$ and $\xi_s \leq 0.5$, and has a minimum of $A_E \approx 140$ at $\xi_s \approx 0.34$ along the ξ_s axis [11]. Evidently, if the ignition threshold is specified as a fixed value of the product $H_s T_s$, this value of ξ_s corresponds to the optimum fuel configuration. However, the assumption that the threshold value of $H_s T_s$ is independent of other implosion parameters would be inadequate in our case because it does not account for the tamping effect of the cold fuel, which depends in particular on the implosion velocity U_{im} (for a fixed ξ_s , the $\langle \rho \Delta r \rangle$ value of the cold DT shell, characterizing its tamping effect, is proportional to $H_s T_s U_{im}^{-2}$). A more thorough analysis [10] reveals that, for $U_{im} \geq 3$ (in units of 10⁷ cm s⁻¹) and $\xi_s \approx 0.3$, the adequate ignition condition is

$$H_s T_s \text{ (g cm}^{-2} \text{ keV)} \approx 0.45 U_{im} \quad (14)$$

From Eqs. (8) and (14) we obtain the following ignition boundary in the (U_{im}, α) parametric plane:

$$\alpha = \left(\frac{E_f}{10 \text{ MJ}} \right)^{1/3} \left(\frac{U_{im}}{10^7 \text{ cm s}^{-1}} \right)^{7/3} \quad (15)$$

This is shown in Fig. 3 with thick full lines for two values of E_f . This scaling is very well confirmed by 1D simulations plotted in Fig. 3 as full circles connected by thin full lines; the simulations started from the assembled fuel configurations and included full physics relevant to the process of ignition.

Targets with fuel parameters above the ignition boundary (15) in the (U_{im}, α) plane do not ignite, while those below it do ignite if there are no additional restrictions on the implosion process. However, important constraints are imposed by the Rayleigh–Taylor instability of the ablator and by inevitable drive asymmetries. These constraints shift downward the position of the ignition boundary in the (U_{im}, α) plane, as illustrated in Fig. 3 with broken lines. Once these constraints are accounted for, one is free to pick up any pair of U_{im} and α values below the ignition boundary as a “working point”, provided that these values can be reached in a 1D implosion.

Following the previous work [12,13], we introduce the limitations due to the Rayleigh–Taylor instability and the drive asymmetries by assuming fixed values of the (IFAR) A_a of the imploding ablator shell of 30 and the radial convergence ratio C_0 of the capsule of 30. In doing so, we suppose that the power pulse consists of a pre-pulse which sets the fuel isentrope for a given value of α , and the main pulse which drives the

cold fuel shell to its implosion velocity U_{im} . The value of A_a that we use here is defined for the time of onset of the main pulse. The convergence ratio C_0 is defined as the ratio R_{caps}/R_s of the initial capsule ablator radius $R_{caps} \equiv R_a$ to the spark radius R_s at ignition. Given the value of the ablator IFAR A_a , the initial inner radius R_g of the solid DT shell can be evaluated as

$$R_g(\text{mm}) = 0.136 A_a^{5/6} \frac{\alpha^{1/2} M_f^{1/3}}{U_{im}} \quad (16)$$

(here M_f is in milligrams, U_{im} in 10^7 cm s^{-1}) by using the following assumptions:

- (a) at the onset of the main pulse, the ablator–fuel mass ratio M'_a/M_f is close to its optimum value $M'_a/M_f \approx 4\text{--}5$ [9], while the inner radius of the fuel shell remains near its initial value R_g ;
- (b) during the main pulse, the compressed ablator material obeys the same equation of state $P = K\alpha\rho^{5/3}$ as the adjacent layer of the DT fuel;
- (c) the fuel is imploded by the main pulse at a constant acceleration U_{im}^2/R_g over one-half of its initial radius R_g .

Assumption (b) is based on the observation that, on the one hand, the adiabatic index of low Z elements is close to $5/3$ at pressures $P \geq 50 \text{ Mbar}$ and, on the other hand, one would prefer to have no density jump at the fuel–ablator interface during the phase of fuel acceleration. A smooth density transition across the fuel–ablator interface allows us to combine the hydrodynamic stability of this interface with a maximum possible thickness of the ablator for a given value of its mass $M'_a \approx (4\text{--}5)M_f$. Note that the properties of realistic ablators may come close to but not quite reach the ideal case assumed here. Conditions (a)–(c) imply that the cold fuel and the compressed ablator have approximately equal IFAR values, $A_f \approx A_a$, at the beginning of the main pulse, a fact that has actually been used in derivation of Eq. (16) (for more details see Ref. [10]).

Taken alone, the condition $A_a = A_f = 30$ does not affect the fuel parameters at ignition and only specifies the values of the initial fuel radius and the ablation pressure. The situation changes, however, after we add a limit on the full convergence

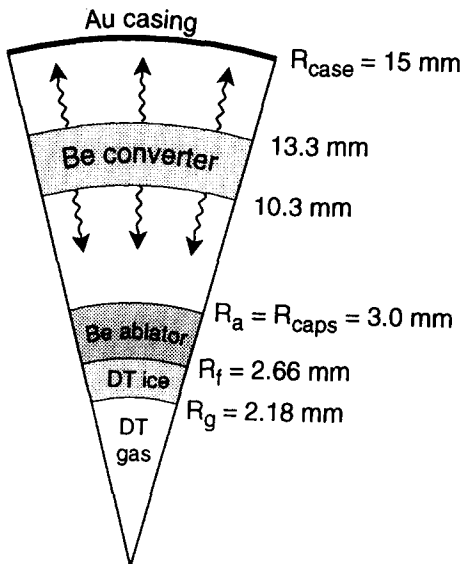


Fig. 5. One-dimensional spherical configuration used as an “energetically” equivalent substitute for the 3D target depicted in Fig. 4: both configurations have roughly the same casing-to-capsule surface area ratios and the same converter masses. The ion energy deposition is modelled as a uniform heating of the entire converter mass.

ratio $C_0 = R_a/R_s$. Assuming an initial solid DT density of $\rho_{r0} = 0.224 \text{ g cm}^{-3}$ and exploiting the condition of mass balance, we obtain a relationship

$$\frac{C_0}{A_a^{5/6}} = 0.622 \left[1 + (1 + b_{af}) \left(\frac{11.2}{A_a} \right)^{5/2} \frac{U_{im}^3}{\alpha^{3/2}} \right]^{1/3} \times \frac{(1 - \xi_s^2)^{5/6} \phi_M^{5/6}}{\xi_s \phi_E^{1/2}} \quad (17)$$

where b_{af} is the ratio between the initial ablator and solid DT volumes; in numerical estimates we assumed $b_{af} = 1$. For any pair of U_{im} and α Eq. (17) yields the value of ξ_s which is no longer the optimum value used in derivation of the ignition boundary (15). The corresponding shift of the ignition boundary, as calculated for $A_a = C_0 = 30$ and values of E_f equal to 300 kJ and 45 kJ, is shown in Fig. 3 with broken lines. As might be expected, the smaller the invested energy E_f , the stronger the effect of stability and symmetry constraints on the ignition threshold.

Now, given the fuel energy $E_f = \eta_h \eta_{caps} E_{dr} = 0.18 \times 0.20 \times 10 \text{ MJ} = 360 \text{ kJ}$, we can determine the fusion capsule dimensions. First of all, we have to choose the values of U_{im} and α . The smaller these values, the higher the target gain or the wider the ignition margin. However, the values of α that are too close to unity require a very delicate pulse shaping, while too low an implosion velocity precludes the formation of the thermonuclear spark [13]. As a reasonable compromise, we select $\alpha = 2$ and $U_{im} = 3 \times 10^7 \text{ cm s}^{-1}$. As is clearly seen in Fig. 3, this combination lies well within the ignition domain for $E_f = 300 \text{ kJ}$, and hence the more so for $E_f = 360 \text{ kJ}$. From Eq. (13) we calculate the fuel mass $M_f = 8 \text{ mg}$. Eq. (16) yields the inner solid DT shell radius $R_g = 2.18 \text{ mm}$; its outer radius R_r is then 2.66 mm.

Maximum hydrodynamic efficiency corresponds to a certain optimum value of the ablator-to-fuel mass ratio M_a/M_f . For the ablator mass M'_a evaporated during the main pulse this optimum corresponds to $M'_a/M_f = (4-5)M_f$ [9]. After we take into account that about 40% of the initial ablator mass M_a evaporates during the prepulse phase, we arrive at a value of $M_a \approx 8M_f$. The simulations described below have been carried out

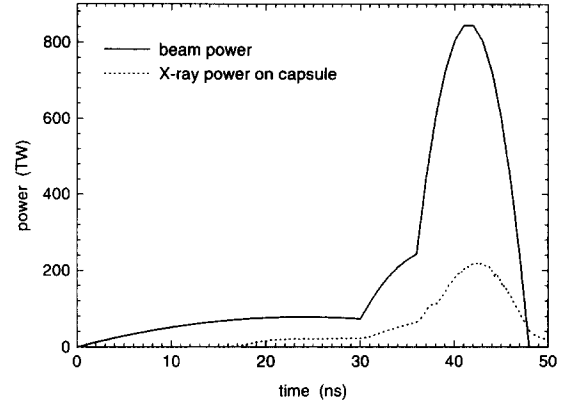


Fig. 6. Total beam power profile (—) formed by adding up four bunches of four different platinum isotopes as described in section 3. The lengths of individual bunches have been optimized for a maximum energy gain of the target shown in Fig. 5. ···, X-ray power absorbed by the fusion capsule.

for a beryllium ablator with initial mass $M_a = 65 \text{ mg}$ and initial density $\rho_{a0} = 1.9 \text{ g cm}^{-3}$, which correspond to a capsule radius $R_a \equiv R_{caps} = 3.0 \text{ mm}$.

2.5. Three-dimensional target scheme

In principal, there may be several hohlraum designs that ensure the required symmetry of capsule irradiation by thermal X-rays. One possibility is to use two-sided illumination of a cylindrical hohlraum by two clusters of ion beams impinging on two converters at the ends of the cylinder [14,15]. Since direct X-rays from such converters would introduce too strong an $l = 2$ asymmetry mode on the capsule, the converters are supposed to be screened with radiation shields, so that the bright rings on the hohlraum walls are formed by the reflected X-rays.

Here we propose another scheme which has no radiation shields inside the hohlraum and is depicted in Fig. 4. The total converter mass $M_{con} = 72 \text{ mg}$ is divided into 12 pieces arranged in two rings above and below the equatorial plane. The 12 ion beams come upon the target in two tiers from six sides. Each beam, having deposited part of its energy in the entrance converter pocket, shoots through the hohlraum cavity and is eventually stopped in the second converter pocket on

the opposite side of the hohlraum. The focal spot radius r_{foc} can be evaluated as

$$r_{\text{foc}} = \left(\frac{M_{\text{con}}}{6\pi \langle \rho l \rangle_{\text{b}}} \right)^{1/2} = 2.06 \text{ mm} \quad (18)$$

where $\langle \rho l \rangle_{\text{b}} \approx 0.09 \text{ g cm}^{-2}$ is the range of 10 GeV ^{209}Bi ions in beryllium at $\rho \approx 0.1 \text{ g cm}^{-3}$, $T \geq 50 \text{ eV}$. Note that this value of r_{foc} is a factor of $\sqrt{3}$ smaller than that in the two-sided illumination scheme.

The hohlraum dimensions given in Fig. 4 have been determined by using the capsule radius $R_{\text{caps}} = 3.0 \text{ mm}$ as the base size, and by eliminating the $l=2$ and 4 asymmetry modes (as described in section 2.1) from the direct X-rays emitted by 12 converter spots on the cylindrical hohlraum wall. Static 3D view-factor simulations have shown that the residual asymmetry in higher ($l, m \geq 6$) angular modes has an initial (at $t=0$) peak-to-valley amplitude of 4%.

2.6. Pulse shaping and results of one-dimensional simulations

1D simulations of the overall target performance have been carried out with the 1D 3-T code DEIRA [16] for the initial target configuration shown in Fig. 5. The input energy $E_{\text{dr}} = 10 \text{ MJ}$ was deposited uniformly over the 72 mg of the Be converter with initial density $\rho_{\text{con}0} = 1.36 \times 10^{-2} \text{ g cm}^{-3}$; its opacity was that of pure beryllium multiplied by a factor of 100. The main goal of these simulations was to demonstrate that ignition and high gain could be achieved with a pulse shape that is consistent with the accelerator and final focus designs.

The initial power W_{pp} and the duration t_{pp} of the prepulse are dictated by the requirement that the first shock of a sufficiently low amplitude has enough time to pass through the ablator and solid DT layers. In our case this corresponds to $W_{\text{pp}} \approx 70 \text{ TW}$ and $t_{\text{pp}} \approx 30 \text{ ns}$. The duration t_{mp} of the main pulse is defined by condition (c) in Section 2.4:

$$t_{\text{mp}} = \frac{R_{\text{g}}}{U_{\text{im}}} = 7.3 \text{ ns}; \quad W_{\text{mp}} \approx \frac{0.6E_{\text{dr}}}{t_{\text{mp}}} = 820 \text{ TW} \quad (19)$$

Here, when evaluating the peak power W_{mp} , we allowed for the fact that the prepulse contains some 40% of the input energy E_{dr} . Power rise from the initial value W_{pp} to the peak value W_{mp} should not go too steeply, so that at least three successive shocks are allowed to pass through the fuel to ensure a fuel entropy corresponding to $\alpha = 2$.

The duration t_{mp} of the main pulse is one of the key parameters which links the target and the accelerator designs. Too severe demands on this parameter may become a major obstacle on the way to a heavy ion ignition facility at an input energy level $E_{\text{dr}} \ll 10 \text{ MJ}$. From Eqs. (19), (16) and (17) we obtain the following scaling for the main pulse duration:

$$t_{\text{mp}} \propto A_{\text{a}}^{5/6} \alpha^{1/2} (\eta_{\text{h}} \eta_{\text{caps}} E_{\text{dr}})^{1/3} U_{\text{im}}^{-8/3} \quad (20)$$

Note that the parameters entering this relationship are not fully independent: the values of U_{im} and α should fall into the ignition domain of the (U_{im}, α) plane as calculated for given C_0 , A_{a} and $E_{\text{r}} = \eta_{\text{h}} \eta_{\text{caps}} E_{\text{dr}}$ values.

Having determined the hohlraum dimensions and the power pulse duration, we actually specify the temperature T_{x} of thermal X-rays in the hohlraum. This temperature may not match the mass and the thickness of the capsule ablator, as calculated in section 2.4, in the sense that the ablator material either is not fully evaporated by the time of ignition or evaporates too early. The ablation rate can, however, be controlled by varying the opacity of the ablator. As already mentioned, in the optimal case the equation of state of the ablator should be as close to that of the DT as possible (for one reason, to alleviate the effects of the Rayleigh–Taylor instability; for another, to attain a higher sound speed to improve the hydrodynamic efficiency of the X-ray drive at $T_{\text{x}} \lesssim 300 \text{ eV}$). We assume that in practice the ablator opacity can be varied independently of its equation of state by admixing some higher Z elements. In the simulations described here we use a simplified approach: beryllium was chosen as the ablator material, and its opacity was varied by a multiplier. Good results presented below have been obtained with the multiplier equal to 0.25, which indicates that actually lithium should be preferred

to beryllium as the base ablator element in our case. In addition, the opacity of the inner edge of the ablator, constituting some 3% of its mass, was increased 100-fold to prevent a premature burn-through of the beryllium.

Fig. 6 shows the pulse shape with which a successful ignition and an energy gain $G = 95$ have been obtained for the 1D target configuration shown in Fig. 5. This pulse profile was found after some limited optimization within the four-isotope charge-symmetric driver scheme described in the next section. The target performance is characterized by the following values of its main parameters.

$T_x = 201$ eV	maximum X-ray temperature in the hohlraum
$\delta_{\text{con}} = 0.18$	energy fraction left in the converter
$\eta_{\text{caps}} = 0.24$	beam-to-capsule energy coupling
$\eta_h = 0.17$	hydrodynamic efficiency of the X-ray drive
$\eta_f = 0.041$	beam-to-fuel energy coupling
$R_s = 0.095$ mm	spark radius at ignition
$\langle \rho r \rangle_{\text{DT,max}} = 2.5$ g cm ⁻²	maximum fuel $\langle \rho r \rangle$
$f_b = 0.35$	fuel burn fraction
$G = 95$	target energy gain

Note that in fact no fine tuning of the DT capsule parameters was needed for successful ignition, although the actual implosion characteristics differ slightly from those evaluated in section 2.4. Since in our 1D simulations we did not account for the beam losses in the converter lids, and because the casing-to-capsule surface area ratio for the target shown in Fig. 4 is about 30 rather than 25, we expect that in reality its energy gain G may be closer to 50–70.

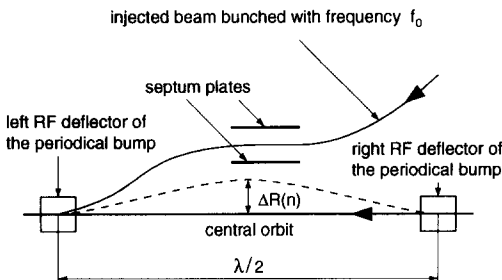


Fig. 7. Scheme of beam injection into the first storage ring.

3. Driver operation scheme with eight species of platinum ions

We employ the driver concept based on accelerating eight different species of platinum ions (four different isotopes, each in two states of singly charged positive and negative ions) in the same linear accelerator complex [6]. Negative ions, when merged with positive ions in the final section of the beam transport channel, reduce the space charge and make it possible to increase the total particle current on target by a substantial factor of 5–10. The linac performance is discussed in a separate paper by

Kapchinsky et al. [17], where it is shown that, provided that the required ion sources are developed, eight species of platinum ions can be accelerated simultaneously in the same linear resonance accelerator, and a current density can be achieved on exit which allows subsequent beam manipulations in the transverse and longitudinal phase space. Here we focus our discussion on the beam handling scheme after the acceleration stage, with a special emphasis on the power pulse tailoring at the target.

We assume that, on leaving the linear accelerator, each ion species has a mean current of 130 mA, with the total current summing up to 1.024 A. Here the beam is a sequence of widely separated bunches about 4.5 cm long, with the distance between the bunches being about 15 m. After the linac, the ion beam passes through a magnetic separation system which deflects each individual ion species into its own first-stage storage ring. Each of the eight first-stage storage rings is 1538 m long and has an aver-

Table 2

Relative deviation $\Delta R(n)$ of the beam orbit at the point of injection into the first storage ring as a function of the revolution number n

n	0	1	2	3	4	5	6	7	8	9	10
$\Delta R(n)$	1	0.4484	-0.5590	-0.880	-0.250	0.50	0.5590	0.0710	-0.250	-0.4484	0

age magnetic field of 0.86 T. Injection into the first ring is performed by using two r.f. deflectors (see Fig. 7), which create a time-varying local distortion of the beam orbit (bump). The values of the relative deviation

$$\Delta R(n) = \frac{1}{2}[\cos(8\pi n f_0 \tau) + \cos(6\pi n f_0 \tau)] \quad (21)$$

of the beam orbit at the point of injection are given in Table 2 as a function of the revolution number n ; here $f_0 = 6$ MHz is the frequency of bunch progression on the exit from the linac, and τ is the revolution period in the ring set equal to $1/20f_0$. Because of the symmetry $\Delta R(10 + n) = \Delta R(10 - n)$ only the first ten revolutions are listed. The distance between the deflectors is supposed to be equal to the half-wavelength of the betatron oscillation at this place. The two deflectors are fed by two generators producing sine-modulated fields with frequencies $3f_0$ and $4f_0$.

Such an injection scheme allows a longitudinal compression of a bunch train by a factor of about 20 to be achieved. The value of the compression factor is determined by the ring length or, more precisely, by the shift of the bunch train after one revolution: if the bunches are shifted by $1/20$ of the interbunch distance (as is assumed in Eq. (21)), the compression factor is 20. Thus, after 20 successive revolutions in the first-stage storage ring, the current of each ion species reaches 2.6 A. The phase volume is conserved here, but the momentum spread (for a coasting beam) increases by a factor of 20 because the beam becomes 20 times shorter. Note that such an increase in the momentum spread has the beneficial effect of increasing the excitation threshold for the microwave instability. The beam energy accumulated in each first-stage storage ring is 400 kJ.

In view of the fact that the beam is already being compressed when injected into the first-stage storage ring, this ring might be called a compression

ring. To avoid confusion, we do not apply this term to the first-stage rings.

Further on, each of the eight ion beams is transported into a corresponding second-stage storage ring (eight rings altogether), which is 5 times shorter than the first, i.e. 308 m long, and has a 5 times higher average magnetic field of 4.3 T. The strength of the magnetic field in dipole magnets is less than about 6 T. Injection into the second storage ring is performed over five turns by stacking the beam along the vertical direction. As a result, the ion current grows fivefold to 13 A. Calculations have shown that during this procedure the vertical emittance increases by a factor of about 7. The beam energy circulating in each second-stage ring is 400 kJ.

At the next stage, the beam is extracted from the second ring in a single turn and cut into four segments of equal length; each of the segments is injected into a separate third stage ring, which is essentially a compression ring. The compression rings have approximately the same length as the second-stage ring and, therefore, are filled by some 25% only. The extraction procedure is repeated three times, each time into a new group of four compression rings. Thus, each of the eight ion species fills 12 compression rings, with their total number adding up to 96. The 12 different compression rings for each ion species correspond to 12 beams coming upon the target (see Fig. 4). The beam energy in each compression ring is 100 kJ, which yields $E_{dr} = 9.6$ MJ for the total energy delivered onto the target.

After all the compression rings have been filled, the process of longitudinal bunching begins. To generate the power pulse required for low entropy compression of the main fuel which is shown in Fig. 6, we take advantage of the fact that there are eight compression rings with eight different ion species

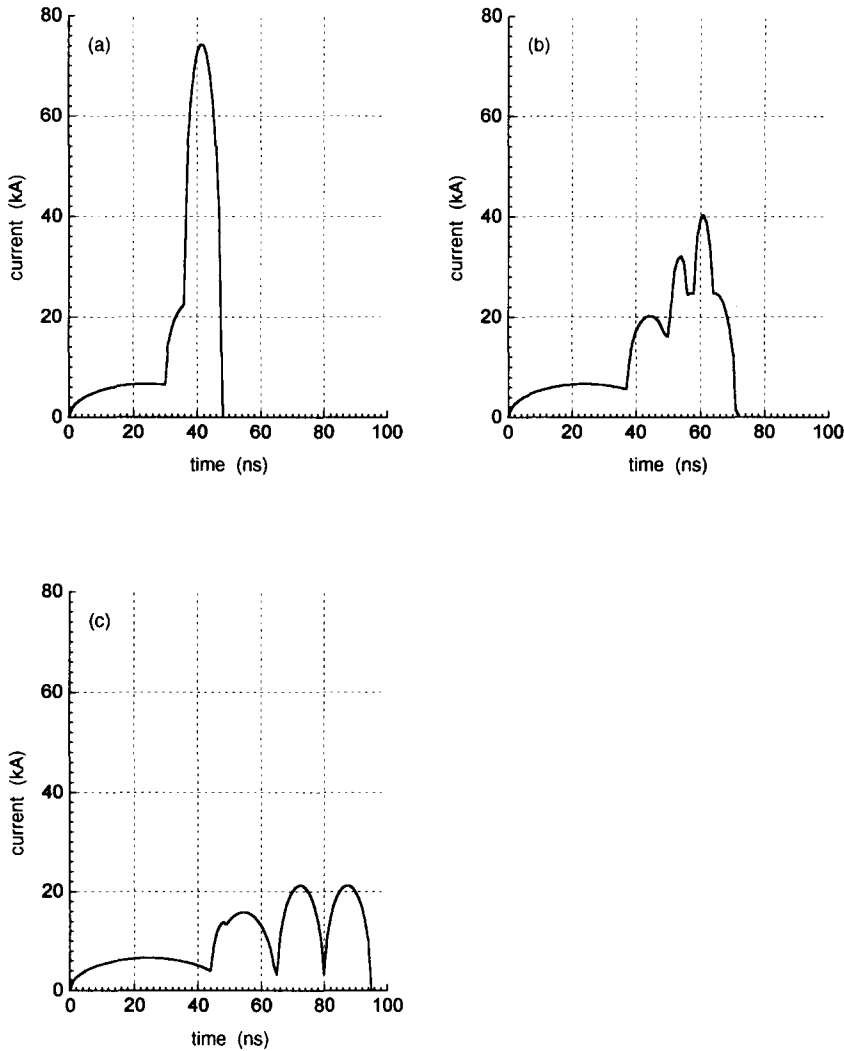


Fig. 8. Temporal dependence of the total particle current summed over 12 incoming beams at different values of the distance s from the target: (a) $s = 0$ m; (b) $s = 75$ m; (c) $s = 150$ m.

along each beam line. To form the long pulse foot of 48 ns duration on the target, we use one pair of compression rings with the heaviest platinum isotope in its two charge states. The corresponding bunch, composed of merged positive and negative ions, will be the slowest and the longest. The low intensity prepulse created in this manner contains 1/4 of the total input energy, i.e. 2.4 MJ, divided equally between the 12 beam lines.

The next pair of rings, containing the next more massive isotope, is used to provide an intermediate power rise by delivering a 18 ns bunch in each of the

12 beams. Again, it contains 1/4 of the total drive energy $E_{dr} = 9.6$ MJ. The last two pairs of rings with the lightest ion species produce the two shortest bunches of 12 ns each, which make up the main portion of the power pulse and contain one-half of the input energy E_{dr} . The lighter isotopes have higher velocities and catch up with the heavier isotopes as they arrive on the target. The four pulse components (bunches) are supposed to be synchronized in such a way that their tails reach the target simultaneously. The longitudinal compression of each of these bunches by factors of 63,

42 and 16 is performed by a conventional r.f. method and is not discussed here. As a result, we obtain the pulse shape shown in Fig. 6, which ignites the target described in the previous section.

When the bunches with comparatively high relative energies of about 1 MeV are merged, a dangerous effect of inelastic intrabeam scattering comes into play, which can cause considerable beam particle losses. This effect is discussed in more detail in a separate contribution by Balabaev et al. [18]. Calculations based on extrapolations of the known charge transfer cross-sections have shown that the particle losses can be kept under about 1%, provided that the external focusing does not allow the mean beam radius to fall below about 2 cm in the storage ring, and below about 6 cm in the final portion (about 25%) of the transport channels.

The final stage of power pulse compression is illustrated in Fig. 8. It is clearly seen how all four types of bunches merge over the last 150 m of the transport channel to form the pulse shape required to ignite the target. It should be noted here that, if maximum bunching had been realized in all four types of the compression rings, a peak power of 960 TW could be reached on the target. Coulomb effects in the beam transport channels have been analysed in the linear approximation by Barkhudaryan et al. [19], who calculated the constraints on the beam current due to the coherent dipole and quadrupole oscillations as well as those due to the non-coherent oscillations. It has been shown that the most stringent limit arises from the coherent quadrupole oscillations because of the rapid frequency growth for these oscillations with the ion current. Nevertheless, under certain conditions that are not difficult to fulfil, the maximum power that can be transported in a charge-symmetric scheme is shown to exceed the maximum power for single-charge beams by a factor of 8–10.

Acknowledgement

This work was supported by the INTAS Grants 93-2571 and 94-1713.

References

- [1] M.M. Sluyter, in Plasma Physics and Controlled Nuclear Fusion Research 1992, Proc. 14th Int. Conf. Würzburg, 1992, Vol. 3, IAEA, Vienna, 1991, paper IAEA-CN-56/B-1-1, p. 3.
- [2] J.D. Lindl, R.L. McCrory and E.M. Campbell, Phys. Today 45 (1992) 32.
- [3] B. Badger, F. Arendt, K. Becker et al., HIBALL—a conceptual heavy ion beam driven fusion reactor study, University of Wisconsin Rep. UWFD-450, 1981; Kernforschungszentrum Karlsruhe Rep. KfK-3202, 1981. B. Badger, K. Beckert, R. Bock et al., HIBALL-II—an improved conceptual heavy ion beam driven fusion reactor study, University of Wisconsin Rep. UWFD-625, 1985; Kernforschungszentrum Karlsruhe Rep. KfK-3840, 1985.
- [4] P.R. Zenkevich, V.S. Imshennik, I.M. Kapchinskii, D.G. Koshkarev, M.D. Churazov and V.G. Shevchenko, Some results of the study on the problem of controlled fusion induced by heavy ions obtained at ITEP, Preprint ITEP-133, 1985 (Institute of Theoretical and Experimental Physics, Moscow) (in Russian).
- [5] M.D. Cable, S.P. Hatchett, J.A. Caird, J.D. Kilkenny, H.N. Kornblum, S.M. Lane, C. Laumann, R.A. Lerche, T.J. Murphy, J. Murray, M.B. Nelson, D.W. Phillion, H. Powell and D.B. Rens, Phys. Rev. Lett. 73 (1994) 2316.
- [6] D.G. Koshkarev, Nuovo Cim. A 106 (1993) 1567.
- [7] D.D.-M. Ho, J.D. Lindl and M. Tabak, Nucl. Fusion 34 (1994) 1081.
- [8] A.I. Larkin, Zh. Eksp. Teor. Fiz. 37 (1959) 264.
- [9] M. Murakami and K. Nishihara, Jpn. J. Appl. Phys. 26 (1987) 1132.
- [10] M.M. Basko, Nucl. Fusion 35 (1995) 87.
- [11] M.M. Basko, On the gain scaling of ICF targets, Fus. Eng. Des. 32–33 (1996) 569.
- [12] C.P. Verdon, R.L. McCrory, R.L. Morse, G.R. Baker, D.I. Meiron and S.A. Orszag, Phys. Fluids 25 (1982) 1653.
- [13] J.D. Lindl, in Proc. Course and Workshop on Inertial Confinement Fusion, Varenna, 1988, Editrice Compositori, Bologna, 1989, pp. 595, 617.
- [14] J.D. Lindl, Nuovo Cim. A 106 (1993) 1467.
- [15] M. Tabak, Les Houches Winter School on Intense Ion Beam and Target Physics for Particle Driven ICF, Les Houches, March 13–17, 1995.
- [16] M.M. Basko, Nucl. Fusion 32 (1992) 1515.
- [17] M.I. Kapchinsky, I.L. Korenev, L.A. Yudin and D.G. Koshkarev, Linac for charge-symmetric four-isotope heavy ion driver, Fus. Eng. Des. 32–33 (1996) 355.
- [18] A.N. Balabaev, Yu.N. Cheblukov and D.G. Koshkarev, The heavy ion losses in charge-symmetric driver due to intrabeam scattering, paper presented at the 7th International Symposium on Heavy Ion Inertial Fusion, Princeton, September 1995.
- [19] A.V. Barkhudaryan, D.G. Koshkarev and A.N. Talyzin, Studies on stability of charge-compensated ion beams, Fus. Eng. Des. 32–33 (1996) 183.